Proceedings of ASME Turbo Expo 2011
GT2011
June 6-10, 2011, Vancouver, British Columbia, Canada

GT2011-45520

NUMERICAL SIMULATIONS OF CONFINED, TURBULENT, LEAN, PREMIXED FLAMES USING A DETAILED CHEMISTRY COMBUSTION MODEL

Massimiliano Di Domenico*
Institute of Combustion Technology
German Aerospace Center (DLR)
Stuttgart, 70771
Germany

Peter Gerlinger
Institute of Combustion Technology
German Aerospace Center (DLR)
Stuttgart, 70771
Germany

Berthold Noll
Institute of Combustion Technology
German Aerospace Center (DLR)
Stuttgart, 70771
Germany

ABSTRACT

In this paper numerical simulations of a confined, high strained jet flame employing a detailed chemistry combustion model are presented. Unlike other configurations available in literature, the geometry under investigation presents the jet axis shifted one side of the confining chamber in order to get non-symmetric recirculation zones and a flame stabilization mechanism based on the recirculation of a high percentage of hot combustion products. Fully three-dimensional unsteady simulations are carried out with finite-rate chemistry effects included by means of a detailed reaction scheme. Turbulence-chemistry interaction is taken into account by employing a presumed PDF approach, which is able to close species source terms by solving two additional transport equations. The use of the hybrid RANS/LES SST-SAS turbulence model is able to include large unsteady turbulent structures according to the local grid size and flow conditions. The approach presented here allows an in-depth investigation of flame stabilization mechanisms, ignition phenomena and influence of recirculation regions on flame stability. Additional simulations adopting simpler combustion models (i.e. Eddy-dissipation Concept) are also presented in order to assess the prediction capabilities of methods widely used in design environments. The paper also includes experimental data while comparison in terms of radial profiles at different heights above the burner are provided.

*Corresponding author (massimiliano.didomenico@dlr.de)

Introduction

During the past different approaches aiming to design low-NOx combustion chambers for stationary gas turbines have been proposed for different degree of success. One of the most promising way to keep emission levels low and high degree of efficiency is the so-called flameless or MILD combustion [1, 2], where a non-swirled, high velocity reacting flow is stabilized by the mixing with a high percentage of hot combustion products. Because of dilution, maximum flame temperature is drastically lowered without compromising the flame stability, as radicals found in the recirculating gases are able to enhance flame propagation speed and to decrease ignition delay times [3]. Thermodynamic analyzes [4] showed that power plants using flameless combustion and combined CCGT cycle with an heat recovery steam generator may able to achieve efficiencies well above 60%. A number of experimental [2, 5, 6] and numerical [7, 8, 9, 10] works dealing with this combustion technology appeared in the literature. Distinguish feature of these systems is a distributed combustion regime, with radicals and intermediate species (CO, H_2) that are detected far downstream the burner exit and uniform radiative fluxes coming from the whole medium. Under these conditions natural gas and light oil seem to have similar behaviors [6] while a flame can be visually detected if heavy oils and coal are burned. By means a well-designed combustion chamber, Li et al. [11] demonstrated that there is a limited range of mass flows under lean conditions that show a distributed reaction region with very low CO and NOx emission indexes. Moreover, even if such configurations are theoretically technically premixed (fuel is injected right before the burner exit), CO and NOx emis-

sion curves are near to those of fully premixed systems. The only exception is represented by the behavior of CO near the lean blow out limit, since CO emissions do not increase as it is normally expected in premixed flames. Hydrogen containing fuels can also burn in flameless regime with NO emissions which are almost independent from the amount of H_2 contained in the fuel [10]. In the work of Lückerath et al. [5] the influence of the inlet velocities and hydrogen content on the CO and NOx emissions in a high pressure FLOX® burner was extensively investigated. It was found that one-digit emission could be achieved for a wide range of air-fuel ratio and high inlet velocities. The addition of hydrogen was able to extend the range of stable operation, although an increase of NOx was observed. High power density could be reached if particular care to the mixing process was paid [12]. Unlike conventional gas turbine combustion chambers, confinement effects are fundamental for establishing a flameless regime, as it was shown in [11]. Wall-near treatment can not be then considered of a secondary importance, as it normally done in standard combustion chambers.

Modeling and designing a combustion chamber where a stable and efficient flameless heat release takes place is far from being trivial. Because of the high strain rates attained in the mixing layer and the intense stirring with hot recirculating gases, a distributed reaction regime is obtained, where most of the turbulent combustion models for gas turbine applications may fail. Detailed chemical kinetics in conjunction with one-dimensional reaction networks were used in the past [13] to investigate combustion emissions and influence of the vitiated coflow in suppressing pollutant formation. The whole process was divided into stirring, ignition, combustion, post-combustion and dilution phase and it was shown that the reduction of the ignition delay time due to radicals available in the recirculating gases was responsible for the flame stabilization mechanism. Detailed CFD analyzes coupled with a two-steps eddy break up model were employed in the past [2]. Those results showed that more detailed chemistry models including hydrogen and CO were needed in order to reproduce experimental temperature profiles. A conserved scalar approach without radiation effects was used in Ref. [14] but the comparison with experimental results reported in the same paper showed that the flamelet approach is unsuited for this kind of combustion regime, as it predicts reaction inside the mixing duct. Conditional Moment Closure (CMC) approach was applied to highly diluted combustion of a CH_4/H_2 mixture [8] with varying O_2 content in the hot coflow (3-9%). The approach was able to give accurate predictions of first order quantities and fair agreement of CO and NO concentrations for all but the case with the lowest O_2 content. Same conclusions were drawn in the work of Christo and Dally [7] where several turbulence and combustion models were applied to the same test case. In both papers the importance of differential diffusion was addressed. To our knowledge, no attempt was done to perform unsteady simulations of flameless combustion in the literature.

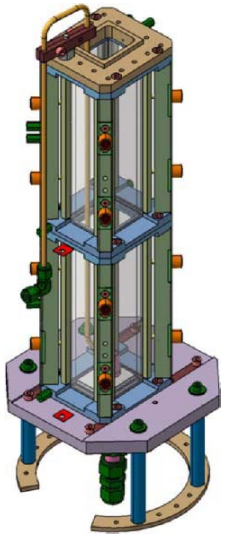

Figure 1: EXPERIMENTAL TEST RIG

In this work a high-strained confined flame is simulated with the use of a detailed chemistry combustion model coupled with a hybrid RANS/LES model for the simulation of large scale turbulent structures. The implementation of detailed chemistry makes possible the investigation of finite-rate chemistry effects and the assessment of the influence of the recirculation zone on the flame stabilization. The hybrid RANS/LES model is able to continuously switch between a RANS-like and a LES-like model according to the local flow conditions and grid size, thus being able to include the transport due to the large turbulent structures. This aspect is of particular important in the test case under investigation, where the entrainment of hot combustion products in the fresh mixture is fundamental for establishing a stable combustion.

Test case under investigation

Experimental setup

The experimental test rig is shown in Fig. 1. As it was already presented in Ref. [15, 16], only few details are given here. The burner consisted of a single jet nozzle with an inner diameter d, and a combustion chamber with a rectangular cross section with edge lengths of $a \times b = 5\ d \times 4\ d$ and an overall height of $h = 60\ d$. The tip of the jet raised $2\ d$ above the burner base plate. The nozzle was positioned at $3.5\ d$ distance from the combustion chamber wall referring to the longer side, and centered at $2\ d$ distance in perpendicular direction. The off-center arrangement was selected to obtain a pronounced recirculation on one side of the jet flow, thereby shaping a flow field in analogy to the inner recirculation zone of a FLOX®combustor. The walls of the combustion chamber were quartz glass plates with reason-

able thickness to minimize heat exchange with the surrounding. As a result, the confined jet flames had mainly contact with hot glass walls, providing a very good optical access in addition.

Both burner and combustion chamber were mounted on a base plate and could be positioned relatively to the stationary laser measurement setups. For quantitative results, laser Raman scattering was applied to the flames and evaluated on an average and single shot basis in order to simultaneously determine the major species concentrations, the mixture fraction and the temperature. The mixing of fuel (methane and hydrogen), air and recirculated exhaust gas, as well as the reaction progress could thus be spatially resolved. Planar velocity fields were measured using particle image velocimetry (PIV).

The numerical simulations are performed under the following conditions:

- atmospheric conditions $p = 1$ atm
- inlet velocity (bulk value) $V_{in} = 150\,{}^{m}/_{\mathrm{s}}$
- inlet temperature (obtained from thermocouple measurements) $T_{in} = 573$ K
- Air/fuel ratio $\phi = 1.4$ (lean regime for methane)

Numerical modeling

The CFD THETA code [17] actively developed at the Institute of Combustion Technology of the German Aerospace Center (DLR) is used for modeling the incompressible Navier-Stokes equations by means a segregated, decoupled, low-Mach approach. A second order, backward difference, non-iterative projection scheme has been used for the time integration.

Turbulence modeling The hybrid RANS/LES SAS-SST turbulence model has been used as turbulent closure in the THETA code. This model has been firstly introduced by Menter et al. [18, 19, 20] and used by other authors in the past [21]. According to their authors, the model is able to continuously switch between the so-called (U)RANS and LES modes according to the local flow conditions and grid cell dimensions. This is a large advantage for the simulation of complex configurations, for those a well designed grid for fully LES can not be guarantee without increasing the grid size beyond any affordable limit. From the theoretical point of view, the SST-SAS turbulence model is base of the $k-L^2$ model rewritten in terms of k and ω. The well established SST model [22] has been adapted

$$\frac{\partial \rho k}{\partial t} + \nabla\left(\rho \mathbf{V} k\right) = \nabla\left(\mu_T \nabla k\right) + S_k \tag{1}$$

$$\frac{\partial \rho \omega}{\partial t} + \nabla\left(\rho \mathbf{V} \omega\right) = \nabla\left(\mu_T \nabla \omega\right) + S_\omega \tag{2}$$

and, besides production and destruction terms already defined in Ref. [22], a key role is played by an additional F_{SAS} terms

$$F_{SAS}^1 = \widehat{\zeta}\kappa S^2 \frac{L_t}{L_{vK}} \tag{3}$$

$$F_{SAS}^2 = C \cdot \frac{2}{\sigma_\phi} k \cdot max\left(\frac{1}{\omega^2}\nabla\omega\cdot\nabla\omega, \frac{1}{k^2}\nabla k\cdot\nabla k\right) \tag{4}$$

$$F_{SAS} = max\left(F_{SAS}^1 - F_{SAS}^2, 0\right) \tag{5}$$

which indeed is to adapt μ_t (acting on ω) to the local flow conditions. This term contains the so-called von Karman length scale based on the ratio of the first to the second velocity derivative (see [23, 24, 18] for details). If the grid and time step are fine enough, the flow equations should be able to resolve small-scale flow structures, thus the SAS term detects the unsteadiness and increases the production of the dissipation rate ω.

Combustion modeling A finite-rate chemistry model able to implement elementary and global reactions is used for this work, as it allows to directly include chemical time scales. At the same time, the general approach used to develop the species transport equations make possible to perform chemical kinetics analysis without changing the solver. The species transport equations can be written in differential form as follows

$$\frac{\partial \rho Y_i}{\partial t} + \nabla\cdot\left(\rho\vec{V}Y_i\right) = \nabla\cdot\left[\left(D_l + D_t\right)\nabla Y_i\right] + S_i^{chem}. \tag{6}$$

A transport equation for the static enthalpy provides the thermodynamic field needed to determine the temperature distribution. The density field is determined according to the incompressible form of the perfect gases law. Concerning the chemistry, a general kinetic scheme with N_s species and N_r reactions yields the following expression for chemical source term

$$S_i^{chem} = M_i \sum_{r=1}^{N_r} \left[k_{f_r}(T) \prod_{j=1}^{N_s} \left(\rho\frac{Y_j}{M_j}\right)^{\nu'_{jr}} \right. \tag{7}$$

$$\left. - k_{b_r}(T) \prod_{j=1}^{N_s} \left(\rho\frac{Y_j}{M_j}\right)^{\nu''_{jr}} \right]. \tag{8}$$

As multiple dynamics associated to this term may yield numerical stiffness, we implement a semi-implicit linearization

$$S_i^{chem}\Big|^{t+1} \simeq S_i^t + \sum_j \frac{\partial S_i}{\partial Y_j}\Big|^t \left(Y_j^{t+1} - Y_j^t\right) \tag{9}$$

An analytical expression for the Jacobian term $\left(\frac{\partial S}{\partial Y}\right)$ is used.

Non-linear behavior of Eq. (7) with respect temperature and species mass fractions also implies a large influence of their fluctuations on the averaged form of Eq. (6). As a closure method based on linearization of this term cannot work [25], an assumed-PDF framework is preferred here. In this approach temperature and species PDF distributions are presumed and are function of their low-order moments, namely mean and variance. Assuming statistical independence of stochastic variables, a split PDF can be formulated

$$P\{T,\mathbf{Y}\} = f_T(T)\, f_Y(\mathbf{Y})\, d\vartheta d\Psi \tag{10}$$

which enables a separate treatment of the terms in Eq. (10). Thus, the averaged form of the source term can be calculated as given in [26].

For the temperature PDF distribution a clipped Gaussian function is assumed [17]

$$f\left(\hat{T};\langle T\rangle,\sigma_T\right) = C_m\delta(T_m) + f_g\left(\hat{T};T_g,\sigma_g\right) + C_M\delta(T_M) \tag{11}$$

$$f_g\left(\hat{T};T_g,\sigma_g\right) = \frac{1}{\sqrt{2\pi\sigma_g}}\exp\left[-\frac{\left(\hat{T}-T_g\right)}{2\sigma_g}\right]. \tag{12}$$

Coefficients of the Dirac's delta in Eq. (11) are proportional to the corresponding clipped areas. According to the distribution's moments, clipping may not be symmetric and moments of the clipped and unclipped distributions may differ. For this purpose a Newton-Rapson method which exploits PDF properties [27] is used to find T_g and σ_g.

Arrhenius functions are averaged with the obtained PDF by a standard Simpson-like quadrature method. In place of look-up tables, integrated functions are cast into a canonical Arrhenius form

$$\left\langle k_{f_r}\left(\hat{T}\right)\right\rangle \simeq A_{f_r}(I_T)\,\langle T\rangle^{\alpha_r(I_T)}\exp\left(-\frac{E_{a_r}(I_T)}{\Re\langle T\rangle}\right) \tag{13}$$

where the interpolated Arrhenius coefficients are function of the temperature fluctuation intensity [28]

$$I_T = \frac{\sqrt{\sigma_T}}{T}. \tag{14}$$

Instead of memory-consuming interpolation tables, in this work polynomial functions of n-th order (up to 14th) in I_T space are used to fit each coefficient [17].

Beside a transport equation for the mean enthalpy, an additional equation for temperature variance [29]

$$\frac{\partial\left(\langle\rho\rangle\sigma_T\right)}{\partial t} + \nabla\cdot\left(\langle\rho\rangle\sigma_T\langle\mathbf{V}\rangle\right) = \nabla\cdot\left(\frac{\mu_t}{Pr_{\sigma_T}}\nabla\sigma_T\right) + S_{\sigma_T} \tag{15}$$

with

$$S_{\sigma_T} = 2\frac{\mu_t}{Pr_{\sigma_T}}\left\|\nabla\langle T\rangle\right\|^2 - C_{\sigma_T}\langle\rho\rangle\frac{\sigma_T}{\tau_t} \tag{16}$$

is solved in order to completely determine the Gaussian distribution of Eq. (11). Eq. (15) is derived from the incompressible form of the enthalpy equation [30] neglecting the influence of the turbulence fluctuations on the temperature-enthalpy relation and temperature-source term correlations.

A multi-variate β-PDF [31]

$$P\left(\widehat{\mathbf{Y}};\langle\mathbf{Y}\rangle,\sigma_Y\right) = \frac{\Gamma\left(\sum_{j=1}^{N_s}\beta_j\right)}{\prod_{j=1}^{N_s}\Gamma(\beta_j)}\prod_{j=1}^{N_s}\left(\widehat{Y}_j\right)^{\beta_j-1}\delta\left(1-\sum_{j=1}^{N_s}\widehat{Y}_j\right) \tag{17}$$

is adopted to take species fluctuations into account. Advantages in using this approach are given in [31, 32] . In Eq. (17) the PDF depends to the so-called turbulent scalar energy

$$\sigma_Y = \sum_{i=1}^{N_s}\left\langle Y_i^{''2}\right\rangle \tag{18}$$

where β_i is function of mean mass fractions and σ_Y

$$\beta_i = \langle Y_i\rangle\left[\frac{\sum_{j=1}^{N_s}\langle Y_j\rangle\left(1-\langle Y_j\rangle\right)}{\sigma_Y} - 1\right] \tag{19}$$

and is limited in the interval $[0,1]$. From β_i and σ_Y the variance of a single species can be obtained from

$$\left\langle Y_j^{''2}\right\rangle = \frac{\langle Y_j\rangle - \langle Y_j\rangle^2}{\sum_j\beta_j + 1}. \tag{20}$$

In order to determine the turbulent scalar energy and hence the species PDF, the following transport equation

$$\frac{\partial\left(\langle\rho\rangle\sigma_Y\right)}{\partial t} + \nabla\cdot\left(\langle\rho\rangle\sigma_Y\langle\mathbf{V}\rangle\right) = \nabla\cdot\left(\frac{\mu_t}{Pr_{\sigma_Y}}\nabla\sigma_Y\right) + S_{\sigma_Y} \tag{21}$$

where

$$S_{\sigma_Y} = 2\langle\rho\rangle\frac{\mu_t}{Pr_{\sigma_Y}}\sum_{j=1}^{N_s}\left\|\nabla\langle Y_j\rangle\right\|^2 - C_{\sigma_Y}\langle\rho\rangle\frac{\sigma_Y}{\tau_t} \tag{22}$$

is solved.

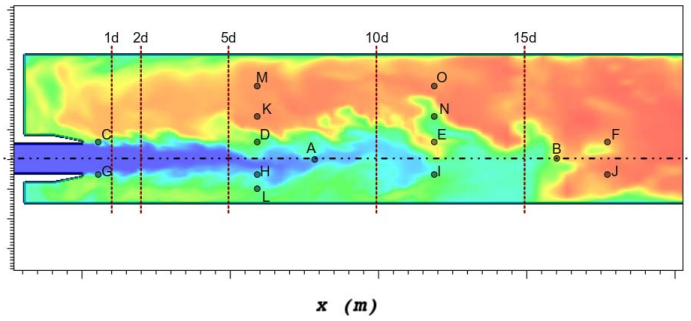

Figure 2: SIMULATION INSTRUMENTATION DETAILS

Coefficients C_{σ_T} and C_{σ_Y} in Eqs. (15) and (21) represent the ratio between dissipation of turbulent kinetic energy and temperature or species fluctuations. After previous comparisons with experimental flames [17] the choice $C_{\sigma_T} = C_{\sigma_Y} = 2.0$ provides a good agreement for jet diffusion flames.

For sake of comparison with established models in industrial environment a global mechanism consisting of three stoichiometric reactions [33] for the combustion of methane and CO is formulated as follows

$$CH_4 + \frac{3}{2}O_2 \rightarrow CO + 2H_2O \tag{23}$$

$$CO + \frac{1}{2}O_2 \rightarrow CO_2 \tag{24}$$

$$CO_2 \rightarrow CO + \frac{1}{2}O_2 \tag{25}$$

This mechanism is used within the framework of an EDC combustion model [34], with reaction rates calculated as minimum between the chemical and turbulent counterparts

$$RR = \min\left(RR_c, RR_t\right) \tag{26}$$

where RR_c is directly derived from an Arrhenius expression

$$RR_c = A_r T^{\alpha_r} \exp\left(-\frac{E_{a_r}}{\Re T}\right) \prod_j [C_j]^{\nu_{jr}} \tag{27}$$

while RR_t is the turbulent reaction rate proposed by Magnussen and Hjertager [34] which is related to the turbulent time scale τ_t obtained from k and ω as solver in the SAS-SST model.

Numerical setup

The domain included in the numerical simulations is represented by the inlet pipe (a length of 10 diameters are included) and the complete squared section combustion chamber. A fully hexaedral grid of about 5.6 million grid elements is used with more points put in the shear layer regions. A reason for the introduction of a large portion of the inlet pipe in the domain is the well known influence of the inlet boundary conditions on the the performance of LES and hybrid RANS/LES turbulence models [35]. By displacing the inlet boundary far from the chamber inlet, the onset of turbulent fluctuations due to pipe walls is provided. At the outlet all but pressure values are extrapolated from the interior points with no ad-hoc non-reflective boundary conditions. As this surface is well far from regions where intense mixing and rotational flow can be found, these simplifications are not expected to have any impact on the results. The simulations are carried out with a time step of $5 \cdot 10^{-7}$s ($CFL_{max} \simeq 1$) and up to three residence times ($t = 0.05$) have been computed in order to get statistically converged means and fluctuation quantities. The methane combustion is described by the reduced GRI mechanism DRM-19 [36] including 19 reacting species and 84 reactions.

Additional monitor points and profiles orthogonal to the main flow directions have been defined (Fig. 2). A series of monitor points are placed along the prolongation of the pipe axis, along the lines on which highest gradients are expected and in the main recirculation region. In Fig. 2 the most interesting locations are superimposed to an instantaneous temperature field. Profiles orthogonal to the pipe axis are extracted at 1d, 2d, 5d, 10d and 15d above the pipe exit, as shown in the same picture.

All CFD simulations have been run on the JUROPA cluster (located in Jülich, Germany) consisting of node having pairs of quad-core Xeon X5570 processors with Infiniband QDR connection. Starting from the unsteady EDC solution presented below, the finite-rate chemistry simulation takes around three weeks on 64 processors (8 nodes) to get converged statistics.

Results

Two-dimensional fields

Instantaneous fields of temperature, velocity and gradient of the progress variable on the chamber symmetry plane as obtained from the detailed chemistry model with the assumed PDF approach are given in Figs. 2 and 3. The velocity vector distribution (Fig. 3a) clearly shows the potential core due to the incoming fresh mixture and the instabilities arising in the region where a strong mixing with the hot combustion products takes place. The intensity of these instabilities increases along the chamber and yields the formation of isolated pockets of fresh mixture surrounded by hot gases (see Fig. 2). A peculiarity of this flame is the asymmetric position of the pipe with respect the chamber axis, asymmetry which is reflected on the large temperature difference between the upper and the lower shear layers. The constant temperature wall boundary condition imposed at the chamber walls is therefore responsible for the large heat

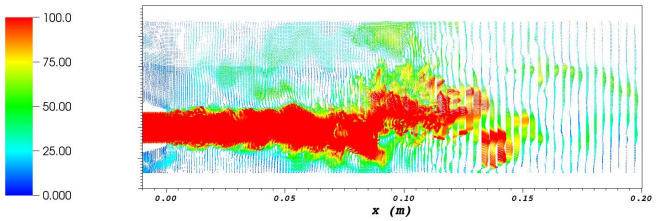

(a) AXIAL VELOCITY VECTOR

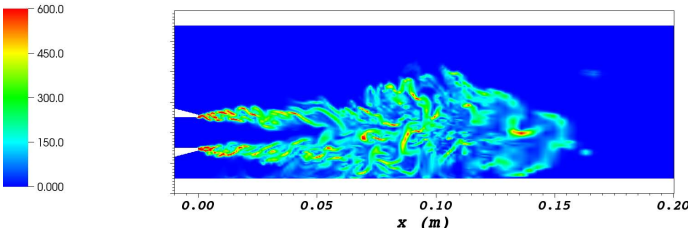

(b) GRADIENT OF THE PROGRESS VARIABLE

Figure 3: INSTANTANEOUS DISTRIBUTIONS ON THE CHAMBER SYMMETRY PLANE

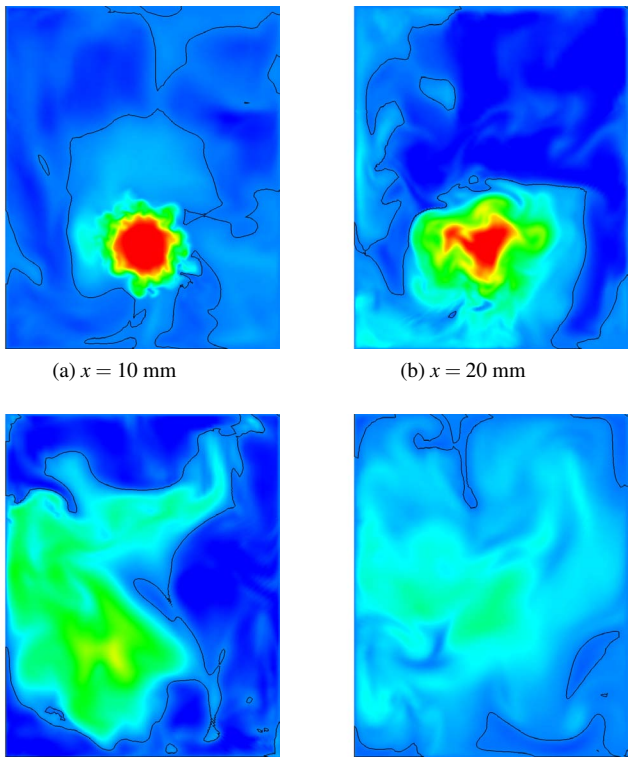

(a) $x = 10$ mm (b) $x = 20$ mm

(c) $x = 50$ mm (d) $x = 100$ mm

Figure 4: DISTRIBUTION OF THE AXIAL VELOCITY AT DIFFERENT HEIGHTS ABOVE THE BURNER. FOR THE LEGEND SEE FIG. 3a.

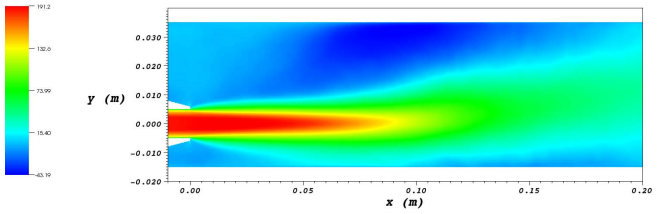

(a) AXIAL VELOCITY

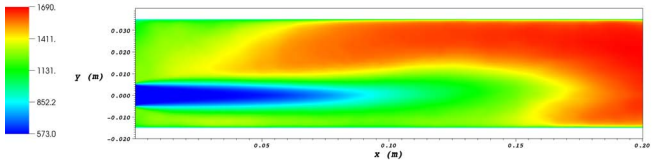

(b) TEMPERATURE

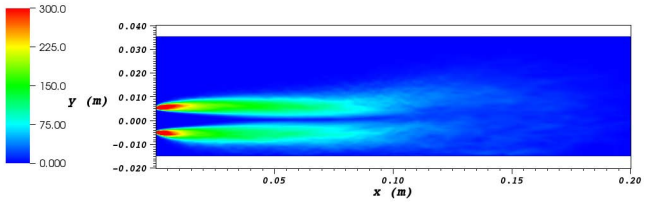

(c) GRADIENT OF THE PROGRESS VARIABLE

Figure 5: AVERAGE DISTRIBUTIONS ON THE CHAMBER SYMMETRY PLANE

losses, as observed in Fig. 2. Figs. 2 and 3a also outlines that there is a "dead" region in the upper left part of the chamber $(x \in [-1.5d, 0], y \in [1d, 3.5d]$ mm) where combustion products are trapped and become significantly colder. In order to emphasize regions where intense mixing and eventually reactions take place, gradients of the progress variable

$$c = 1 - \frac{\mathrm{CH_4}}{\mathrm{CH_4}|_{in}} \tag{28}$$

are shown in Fig. 3b. From the plot it is clearly observed that the mixing process does not take place along a single flame front but in local sheets discontinuously distributed. The layer orientation also changes according to the region considered: while near the pipe exit highest gradients are orthogonal to the $x-$axis, downstream the layer orientation becomes more chaotic with highest gradients parallel to this direction.

Figure 4 shows the instantaneous axial velocity on slices taken at four heights above the pipe exit. The black line links all points at $V_x = 0$, thus delimiting the recirculation region. As expected, a complex pattern is observed with several recirculating regions spread around the central jet. Although recirculating

gases are mainly found in the upper region of the combustion chamber, strong negative velocities also appear in the lower region. Another important feature of this zone is the intermittency of the recirculation, as it can be observed if Figs. 4b and 4c are compared.

Averaged fields are given in Fig. 5 for velocity, temperature and gradient of the progress variable. The axial velocity distribution clearly shows the potential core structure typical of unconfined and confined jets. The asymmetric position of the pipe with respect to the chamber has an impact on the core jet which is indeed bent toward the farthest wall. According to the temperature distribution shown in Fig. 5b a non-symmetric hot zone is obtained. While a very thin flame front is observed in the lower shear layer, the upper recirculation zone shows peak temperatures away from the region where the mixing takes place. The dead zone introduced above experiences a significantly lower temperature for the reasons explained above. The penetration of fresh mixture is about 17 jet diameters, a very low value if compared to free jet configurations.

The gradient of averaged progress variable are plotted in Fig. 5c. Maximum values are smaller than what observed in the instantaneous distribution and are exclusively located near the pipe exit. Strong fluctuations and mixing layer instabilities also yield a very thick mean mixing and reaction layer.

1-D profiles

A detailed validation of the combustion model against experimental data presented in a companion paper [16] in terms of normalized profiles at different locations above the pipe exit, as shown in Fig. 2.

The averaged axial and transverse velocity profiles at the five different locations are plotted in Figs. 6a and 6b. At $x = 1$ d an almost perfect agreement with the PIV measurements is achieved, showing that boundary conditions are well posed. It is worth to point out that the simulations performed in this paper do not introduce any kind of synthetic turbulence at the inlet (as proposed in Ref. [35]). Thus, the agreement achieved by the simulations demonstrate that hybrid LES/RANS models do not need a special treatment at inlet boundaries. The agreement remains excellent until $x = 10$ d, where first discrepancies appear. The fact that even transverse velocities are well reproduced is remarkable since a large difference between axial and transverse momentum exists. Kinematic field predictions do not seem to be affected by the combustion model, as both the simple EDC and the more detailed finite-rate combustion (hereafter FRC) models give profiles lying within the same degree of accuracy. First differences start to appear at $x = 15$ d with the detailed combustion model able to better follow the experimental trend.

Averaged progress variable and temperature profiles are given in Figs. 6c and 6d. For both quantities the differences between the EDC and finite-rate combustion models are clearly observed. Referring to Fig. 6c, at lower locations ($x = 1, 2$ d) both models are able to predict flame width and propagation. Starting from $x = 5$ d the EDC model over predicts the reaction rate while the detailed chemistry model is able to follow the Raman measurements. Discrepancies observed at the last location ($x = 15$ d) can be related to an insufficient grid resolution, as the mesh density exponentially decreases from the pipe exit towards the outflow. Temperature profiles (Fig. 6d) confirms the accuracy of the detailed combustion model with excellent predictions at all locations. It is worth to observe while the EDC model is based on the transport of few species (oxidizer, fuel and combustion products), it is able to reach the correct thermodynamical equilibrium, as the agreement with the experiments in the upper part of the temperature profiles demonstrate.

Rms profile of velocity and progress variable are shown in Fig. 7. The rms profiles of both velocities at $x = 1$ and 2 d do not seem to be affected by the combustion model as both EDC and FRC approaches are able to reproduce peak position and values. Further downstream ($x \geq 5$ d) no clear trend can be recognized, with some regions whether the FRC model or the EDC model are able to give accurate predictions of the rms values.

Figure 7c shows the rms value of the progress variable calculated as follows

$$\left[\overline{(c")^2}\right]^{\frac{1}{2}} = \frac{\left[\overline{\left(Y"_{\mathrm{CH_4}}\right)^2}\right]^{\frac{1}{2}}}{Y_{\mathrm{CH_4}}|_{inlet}} \tag{29}$$

Predictions given by the FRC model (green dashed line) are in good agreement with the experimental data. In all plots both peak position and level are correctly predicted. The bimodal distribution experimentally observed until $x = 10$ d is also reproduced. Some discrepancies are observed at $x = 1$ d for $y < 0$ where the rms peak is over predicted. An excellent agreement is also obtained at $x = 15$ d.

Predictions given by the EDC combustion model are given in the same figure for comparison. Large discrepancies between the prediction given by the EDC model and the experimental data can be observed at locations higher than 1 d. While the measurements at $x = 10$ d still show a bimodal distribution, the simulation adopting the simplified EDC model predicts a single peak with values largely above the experimental levels. On the other hand, at $x = 15$ d the damping of progress variable fluctuations is largely over predicted.

Time behavior analysis

In this Section a detailed analysis of the flame regime at different location of the combustion chamber is presented and discussed. To this purpose data extracted at the locations shown in Fig. 2 are compared with laminar free flame calculations performed with the open-source software Cantera [37] adopting the

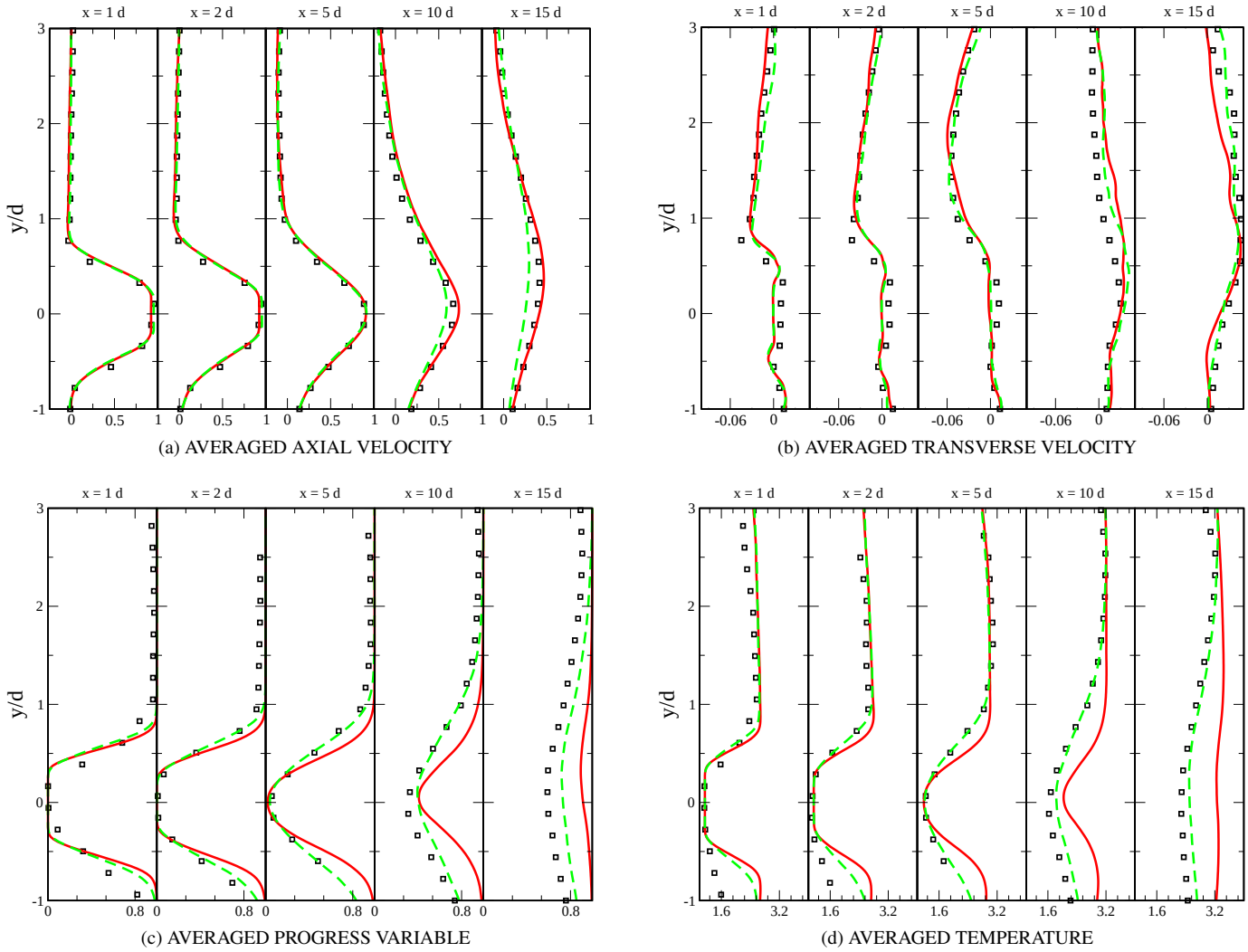

Figure 6: COMPARISON WITH EXPERIMENTAL DATA - NORMALIZED AVERAGED QUANTITIES (SYMBOLS: EXPERIMENTS, SOLID LINE: EDC MODEL, DASHED LINE: DETAILED CHEMISTRY WITH ASSUMED PDF MODEL)

GRI 3.0 mechanism [38], which is by far more comprehensive than its reduced version (DRM 19) used in the CFD calculations. However, we do not expect any difference concerning the laminar free flame calculations, as both mechanisms were validated for these configurations. As it is known that hot recirculating gases play an important role in the investigated configuration, these calculations are performed with a variable amount of hot combustion products that are adiabatically mixed to the inlet fresh mixture, as sketched in Fig. 8. Recirculation ratios ranging from 0% up to 50% (step 10%) are simulated and results are plotted on an H_2O-CO_2 mass fraction space.

Figure 9 shows the laminar flame and monitor point data for several locations in the combustion chamber. In all plots six lines for recirculation ratios 0,10,20,30,40 and 50% are shown. The origin of each line represents the initial mixture condition (origin of the axis if no recirculation is considered, higher CO, H_2O values otherwise) while the other end point is determined by thermodynamic equilibrium. Since the mixing between fresh gases and hot combustion products is assumed to be adiabatic, all calculations reach the same point. The line which would join the origin of the diagram with the equilibrium location would give all CO_2-H_2O locations where only mixing between the fresh mixture and hot combustion products takes place. On the other hand, any location above this line (and below the calculation at 0% recirculation rate) would represent a fluid particle where, at least partially, combustion is taking place.

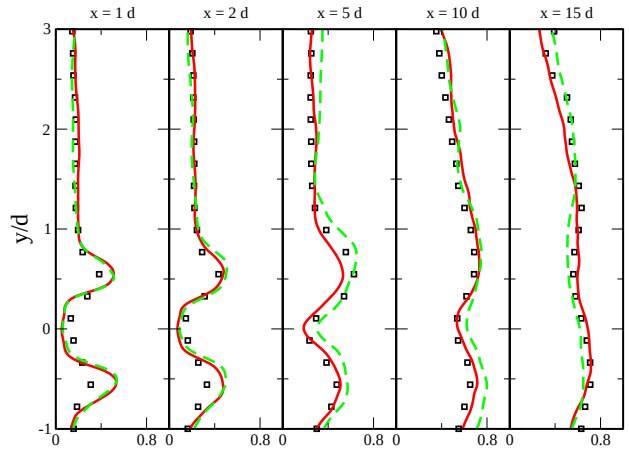

(a) RMS OF AXIAL VELOCITY

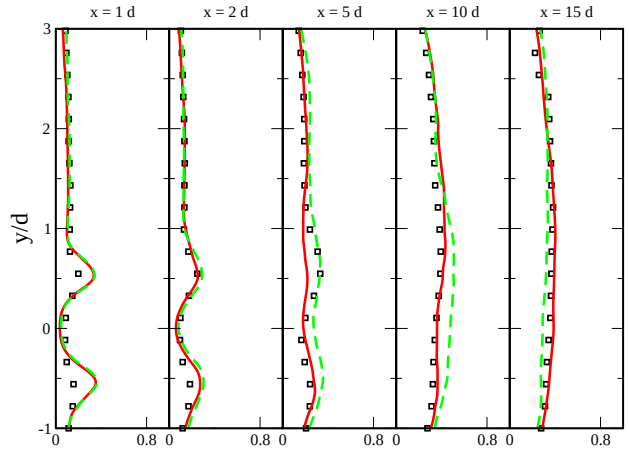

(b) RMS OF RADIAL VELOCITY

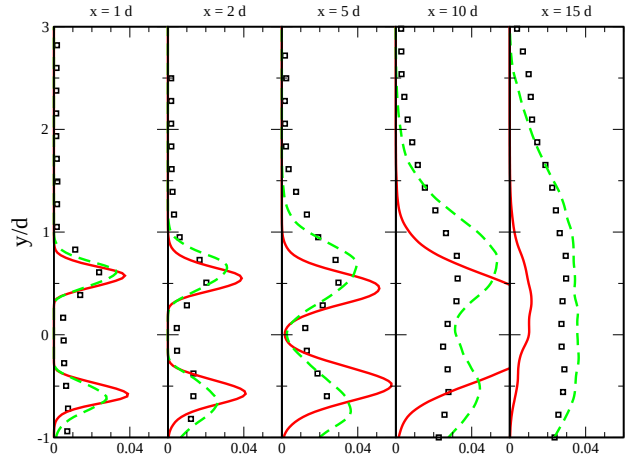

(c) RMS OF PROGRESS VARIABLE

Figure 7: COMPARISON WITH EXPERIMENTAL DATA - NORMALIZED RMS QUANTITIES (SYMBOLS: EXPERIMENTS, SOLID LINE: EDC MODEL, DASHED LINE: DETAILED CHEMISTRY WITH ASSUMED PDF MODEL)

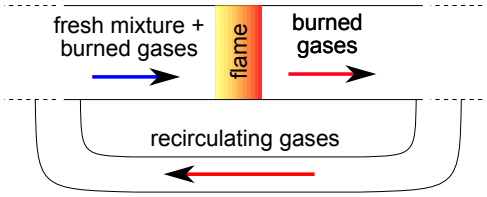

Figure 8: REPRESENTATION OF A LAMINAR PREMIXED FLAME CONFIGURATION WITH RECIRCULATION

Data extracted from three monitor points placed on the prolongation of the jet axis are shown in Fig. 9a. It can be seen that all samples from the point nearest to the pipe exit lie on the mixing line, i.e. no reacting pockets are observed. Although most of them show CO_2 and water concentrations well below the equilibrium values, there is a non-negligible amount of samples near the equilibrium condition. At 16 d above the burner larger spreading of the sample conditions is observed, with all points showing a degree of mixing with hot gases higher than 50%. The degree of scattering also depends on the CO_2 mass fraction, with a broader sample distribution observed for $Y_{CO_2} < 0.06$. Samples with higher CO_2 concentrations are concentrated along the laminar flame profile, meaning that most of them are pockets of burning mixture. At the highest location given in the plot ($x = 24$ d) almost all samples are in equilibrium conditions with only very few burning samples.

A comparison of samples extracted from three points placed in the upper shear layer can be seen in Fig. 9b. Samples belonging to the nearest location are mainly on the mixing line, although some reacting spots can be detected at high CO_2 concentrations (i.e. high temperature). At $x = 12$ d all thermodynamic conditions range from mixing-only to burning mixture are observed. It is worth to note that samples move away from the mixing line as CO_2 increases, unlike what it is observed for point D. Thus, at this stage the mixing process between hot and cold flow particles promotes auto-ignition with no inert samples available. At monitor point F a degree of recirculation which in some cases approaches 50% is shown. As in Fig. 9a, samples with higher CO_2 concentrations are aligned along the laminar free flame solution.

Figure 9c shows data extracted from monitor points placed along the lower shear layer at the same heights as for Fig. 9b. When compared to the latter it can be seen that the lower locations (D, H) have similar thermodynamic conditions, although the scattering of the H samples is slightly higher. Some differences are also observed for the height $x = 12$ d (point E and I), in particular in the tail of distribution at low CO_2 with point E showing a large number of samples with lower CO_2 and water mass fractions. The asymmetric behavior of the flame is clearly seen if samples from point F and J are compared, since the latter have most of samples in equilibrium conditions.

The remaining plots (Figs. 9d-9f) put together monitor

points lying at the same height above the pipe exit but at different distance from the jet axis. When Figs. 9d ($x = 6$ d) and 9e ($x = 12$ d) are compared, effects of the entrainment of hot products into the jet at the downstream location can be clearly seen. As height increases the mixture become more reactive and samples are more scattered. Moreover, almost no inert pockets are observed at CO_2 concentrations near equilibrium ($Y_{CO_2} > 0.08$). The last plot (Fig. 9f) is a comparison between monitor points K and L which are placed above and below the jet axis. The differences at low CO_2 mass fractions are due to larger structures present in the upper recirculation zone which are responsible for entrainment of fresh mixture pocket in the hot zone. This in turns promotes the reactivity of the samples (measured by the scattering of the distribution) while in the lower region the diagram demonstrates that a mixing-only process takes place.

Conclusions

In this work hybrid LES/RANS simulations of a high strained, turbulent premixed flame have been performed and results deeply investigated. It has been found that the coupling of the SST-SAS model with a finite-rate chemistry combustion model is able to reproduce experimental observations and measurements, as both averaged and rms values are in excellent agreement with the PIV and Raman data. On the other hand, predictions given by the EDC model do not always match the experimental data since finite-rate chemistry effects like extinction and re-ignition play a fundamental role in the case under investigation. It has been also demonstrated that the algorithm is able to give insights in the flame stabilization mechanism and combustion regime. By means a comparison with laminar free flame calculations, samples taken from several points in the combustion chamber regions have been investigated and conclusions about the influence of the recirculating gases could be drawn. It can be then concluded that although expensive, the unsteady finite-rate chemistry model represents a unique way to investigate flame regimes and flame-flow interaction within combustion devices.

Acknowledgments

The authors would like to acknowledge A. Fiolitakis for the interesting discussions on laminar premixed flames, T. Panne for providing the initial computational grid and C. Beck and W. Krebs from Siemens Energy for their technical support. The Jülich Supercomputing Centre is also acknowledged for the computational time provided under the NIC project number 3793. Financial support has been provided by the Land Baden-Württemberg under the contract BW L 43GV within the scope of the KW21 project.

References

[1] Wünning, J. A., and Wünning, J. G., 1997. "Flameless oxidation to reduce thermal no-formation". *Progress in Energy and Combustion Science,* **23**(1), pp. 81 – 94.

[2] Weber, R., Orsino, S., Lallemant, N., and Verlaan, A., 2000. "Combustion of natural gas with high-temperature air and large quantities of flue gas". *Proceedings of the Combustion Institute,* **28**(1), pp. 1315 – 1321.

[3] Levy, Y., Sherbaum, V., and Erenburg, V., 2007. "The role of the recirculating gases at the mild combustion regime formation". *ASME Conference Proceedings,* **2007**(47918), pp. 271–278.

[4] Camporeale, S. M., and Fortunato, B., 2007. "Thermodynamic analysis of semi-closed gas turbine combined cycles with high temperature diluted air combustion". *ASME Conference Proceedings,* **2007**(47926), pp. 459–464.

[5] Lückerath, R., Meier, W., and Aigner, M., 2007. "Flox® combustion at high pressure with different fuel compositions". *ASME Conference Proceedings,* **2007**(47918), pp. 241–249.

[6] Weber, R., Smart, J. P., and vd Kamp, W., 2005. "On the (mild) combustion of gaseous, liquid, and solid fuels in high temperature preheated air". *Proceedings of the Combustion Institute,* **30**(2), pp. 2623 – 2629.

[7] Christo, F., and Dally, B., 2005. "Modeling turbulent reacting jets issuing into a hot and diluted coflow". *Combustion and Flame,* **142**(1-2), pp. 117 – 129.

[8] Kim, S. H., Huh, K. Y., and Dally, B., 2005. "Conditional moment closure modeling of turbulent nonpremixed combustion in diluted hot coflow". *Proceedings of the Combustion Institute,* **30**(1), pp. 751 – 757.

[9] Mancini, M., Weber, R., and Bollettini, U., 2002. "Predicting nox emissions of a burner operated in flameless oxidation mode". *Proceedings of the Combustion Institute,* **29**(1), pp. 1155 – 1163.

[10] Yu, Y., Gaofeng, W., Qizhao, L., Chengbiao, M., and Xianjun, X., 2010. "Flameless combustion for hydrogen containing fuels". *International Journal of Hydrogen Energy,* **35**(7), pp. 2694 – 2697. 2008 International Hydrogen Forum (HyForum2008), 2008 International Hydrogen.

[11] Li, G., Gutmark, E. J., Overman, N., Cornwell, M., Stankovic, D., Fuchs, L., and Milosavljevic, V., 2006. "Experimental study of a flameless gas turbine combustor". *ASME Conference Proceedings,* **2006**(42363), pp. 793–804.

[12] Lammel, O., Schütz, H., Schmitz, G., Lückerath, R., Stöhr, M., Noll, B., Aigner, M., Hase, M., and Krebs, W., 2010. "Flox® combustion at high power density and high flame temperatures". *Journal of Engineering for Gas Turbines and Power,* **132**(12), p. 121503.

[13] Rao, G. A., Levy, Y., and Gutmark, E. J., 2008. "Chemical kinetic analysis of a flameless gas turbine combustor".

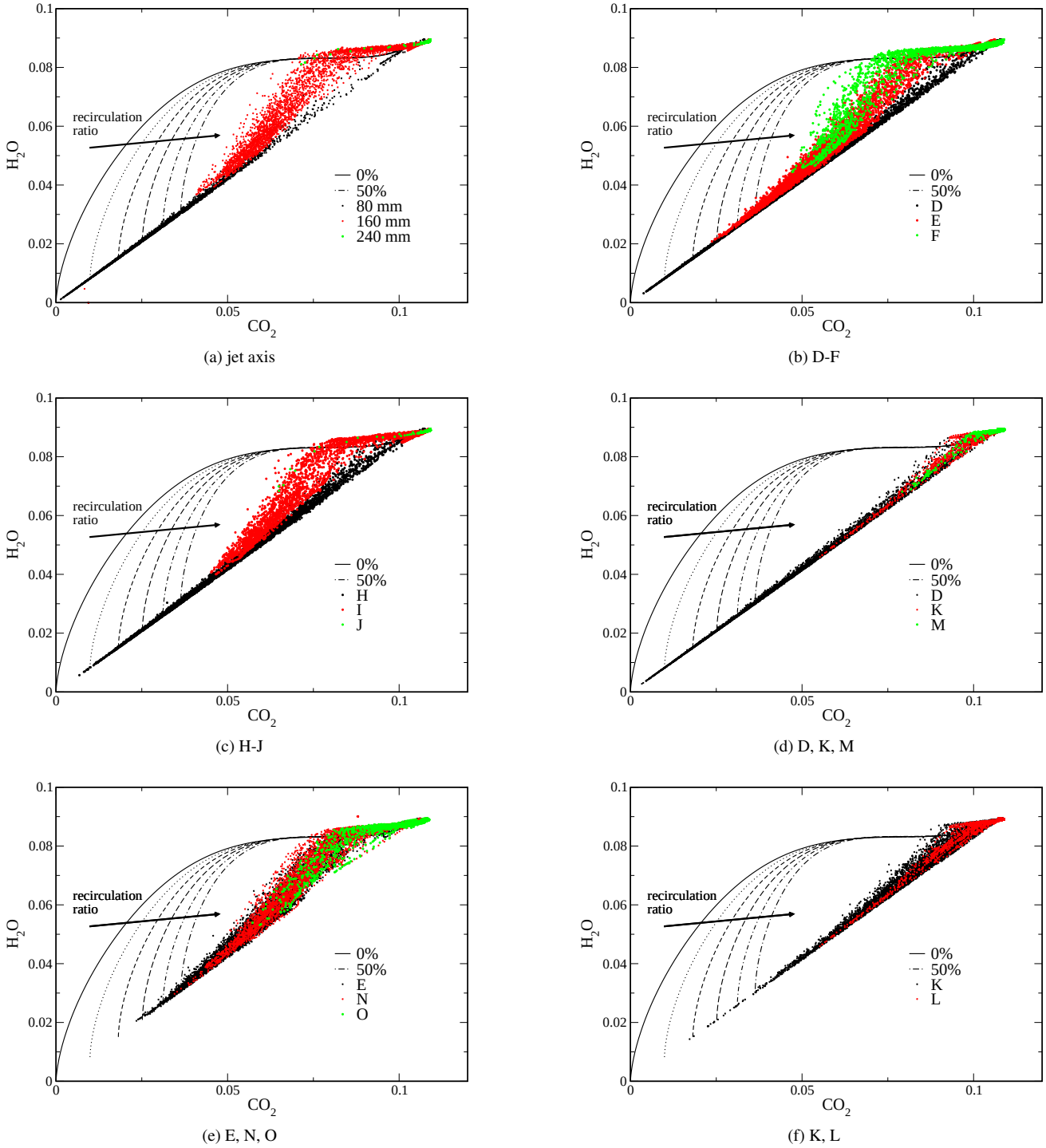

(a) jet axis

(b) D-F

(c) H-J

(d) D, K, M

(e) E, N, O

(f) K, L

Figure 9: H_2O-CO_2 MASS FRACTION DIAGRAMS FOR DIFFERENT MONITOR POINTS AS GIVEN IN FIG. 2. LINES: LAMINAR FREE FLAME CALCULATIONS, DOTS: MONITOR POINT DATA.

ASME Conference Proceedings, **2008**(50619), pp. 487–496.

[14] Vaz, D. C., Borges, A. R. J., van Buijtenen, J. P., and Spliethoff, H., 2004. "On the stability range of a cylindrical combustor for operation in the flox regime". *ASME Conference Proceedings,* **2004**(41669), pp. 511–516.

[15] Di Domenico, M., Beck, C., Lammel, O., Werner, K., and Noll, B., 2011. "Experimental and numerical investigation of turbulent, lean, high-strained, confined, jet flames". *AIAA paper*. submitted.

[16] Lammel, O., Stöhr, M., Kutne, P., Dem, C., Meier, W., and Aigner, M., 2011. "Experimental analysis of confined jet flames by laser measurement techniques". *ASME Conference Proceedings,* **2011**(45111).

[17] Di Domenico, M., 2008. "Numerical Simulation of Soot Formation in Turbulent Flows". Phd thesis, University of Stuttgart.

[18] Menter, F., and Egorov, Y., 2005. "A Scale-Adaptive Simulation Model using Two-Equation Models". *AIAA paper 2005-1095*.

[19] Menter, F., and Egorov, Y., 2005. "A Scale-Adaptive Simulation Model using Two-Equation Models". *AIAA paper 2005-1095*.

[20] Menter, F., and Egorov, Y., 2006. "SAS Turbulence Modeling of Technical Flows". In *Direct and Large-Eddy Simulation*, E. Lamballais, R. Friedrich, B. Geurts, and O. Métais, eds., Vol. VI. Springer Netherlands.

[21] Davidson, L., 2006. "Evaluation of the SST-SAS Model: Channel Flow, Asymmetric Diffuser and Axy-symmetric Hill". In Proceedings of the ECCOMAS CFD 2006 Conference, P. Wesseling, E. Onate, and J. Periaux, eds.

[22] Wilkox, C., 2004. *Turbulence Modeling for CFD*, second ed. DCW Industries.

[23] Egorov, Y., and Menter, F., 2008. "Development and application of SST-SAS turbulence model in the DESIDER project". In *Adwances in Hybrid RANS-LES Modelling*, S.-H. Peng and W. Haase, eds. Springer Verlag Beriln Heidelberg, pp. 261–270.

[24] Menter, F. R., 2009. "Review of the shear-stress transport turbulence model experience from an industrial perspective". *International Journal of Computational Fluid Dynamics,* **23**(4), pp. 305–316.

[25] Gaffney, R., White, J., Girimaji, S., and Drummond, J., 1994. "Modeling Temperature and Species Fluctuations in Turbulent, Reacting Flow". *Computing Systems in Engineering,* **5**(2), pp. 117–133.

[26] Gerlinger, P., Noll, B., and Aigner, M., 2005. "Assumed PDF Modeling and PDF Structure Investigation Using Finite-Rate Chemistry". *Progress in Computational Fluid Dynamics,* **5**(6), pp. 334–344.

[27] Pope, S., 2000. *Turbulent Flows*. Cambridge university press.

[28] Baurle, R. A., 1995. "Modelling of Turbulent Reacting Flows with Probability Density Functions for Scramjet Applications". PhD thesis, North Carolina State University.

[29] Gerlinger, P., Möbus, H., and Brüggemann, D., 2001. "An Implicit Multigrid Method for Turbulent Combustion". *Journal of Computational Physics,* **167**, pp. 247–276.

[30] Kuo, K., 1986. *Principles of Combustion*, first ed. A Wiley-Interscience Publication.

[31] Girimaji, S., 1991. "Assumed $beta$-pdf Model for Turbulent Mixing: Validation ad Extension to Multiple Scalar Mixing". *Combustion Science and Technology,* **78**, pp. 177–196.

[32] Girimaji, S. S., 1993. Simulations of Diffusion-Reaction Equations with Implications to Turbulent Combustion Modeling. ICASE Report 93-69, NASA - Langley Research Center.

[33] Nicol, D. G., Malte, P. C., Hamer, A. J., Roby, R. J., and Steele, R. C., 1999. "Development of a five-step global methane oxidation-no formation mechanism for lean-premixed gas turbine combustion". *Journal of Engineering for Gas Turbines and Power,* **121**(2), pp. 272–280.

[34] Magnussen, B., and Hjertager, B., 1976. "On mathematical modelling of turbulent combustion with special emphasis on soot formation and combustion.". In Proceedings of the 16th International Symposium on Combustion, The Combustion Institute, pp. 719–729.

[35] Klein, M., Sadiki, A., and Janicka, J., 2003. "A digital filter based generation of inflow data for spatially developing direct numerical or large eddy simulations". *Journal of Computational Physics,* **186**(2), pp. 652 – 665.

[36] Frenklach, M., Wang, H., Goldenberg, M., Smith, G., Golden, D., Bowman, C., Hanson, R., Gardiner, W., and Lissianski, V., 1995. Gri-mech—an optimized detailed chemical reaction mechanism for methane combustion. Tech. Rep. Report No. GRI-95/0058, Gas Research Institute Topical Report, November.

[37] Goodwin, D., 2009. Cantera: An object-oriented software toolkit for chemical kinetics, thermodynamics, and transport processes.

[38] Smith, G., Golden, D., Frenklach, M., Moriarty, N., Eiteneer, B., Goldenberg, M., Bowman, C., Hanson, R., Song, S., Gardiner, W.C., J., Lissianski, V., and Qin, Z., 1999. Gri mech 3.0. http://www.me.berkeley.edu/gri_mech/.